Room-temperature ferromagnetism via unpaired dopant electrons and *p*-*p* coupling in carbon-doped In$_2$O$_3$: Experiment and theory

R. J. Green,[1,*] D. W. Boukhvalov,[2] E. Z. Kurmaev,[3] L. D. Finkelstein,[3] H. W. Ho,[4] K. B. Ruan,[4] L. Wang,[4] and A. Moewes[1]

[1]*Department of Physics and Engineering Physics, University of Saskatchewan, 116 Science Place,*
Saskatoon, Saskatchewan S7N 5E2, Canada
[2]*School of Computational Sciences, Korea Institute for Advanced Study, Hoegiro 87, Dongdaemun-Gu, Seoul 130-722, Korean Republic*
[3]*Institute of Metal Physics, Russian Academy of Sciences-Ural Division, 620990 Yekaterinburg, Russia*
[4]*Division of Physics and Applied Physics, School of Physical and Mathematical Sciences,*
Nanyang Technological University, Singapore 637371, Singapore

Observations of magnetism in semiconductors doped with nonmagnetic atoms (C, N, etc.) show promise for spintronics applications, but pose an interesting challenge for conventional theories of magnetism. In this work, the magnetic semiconductor carbon-doped In$_2$O$_3$ is studied using theoretical and experimental techniques. Density-functional theory calculations predict that ferromagnetism can exist near room temperatures when substitutional carbon atoms have a formally unpaired 2p electron that does not participate in bonding. The unpaired 2p electrons lead to an impurity band near the Fermi level and consequent enhanced density of states which accommodates a strong p-p coupling between local magnetic moments. The unpaired electrons and ferromagnetic coupling are found to arise from a combination of interstitial and substitutional carbon atoms in close proximity. Finally, experimental measurements on samples with varying magnetic properties verify the importance of both strong C 2p character at the Fermi level and strong C 2sp-In 4d hybridization for yielding room-temperature ferromagnetism. These results shed light on the interesting field of nonmagnetic dopants inducing ferromagnetism in semiconductors.

I. INTRODUCTION

The research interest in dilute magnetic semiconductors (DMSs) has been very intense for over a decade, and the intriguing properties of these materials continue to elude clear explanations with consensual acceptance in the scientific community. The reasons for the strong interest are twofold: a full understanding of DMSs could lead to materials usable for spintronic computing,[1] and the unique magnetic properties of the materials are interesting from a condensed-matter perspective as well. For example, it is now commonly found that low concentrations of magnetic 3d dopant atoms can lead to semiconductors exhibiting persistent ferromagnetism even at room temperatures,[2] but a single clear explanation for how this exists has yet to be agreed upon. The impurity atoms are spaced beyond the percolation thresholds for mechanisms like superexchange,[3] and pure carrier mediation of the exchange does not seem likely in most cases either.[4] Recent theories involving impurity bands formed by vacancies or other defects which can exhibit spin split behavior seem promising,[3,5] but are not yet mature and fully tested.

Without doubt, the field of 3d doped semiconductors and oxides is very intriguing. However, the idea of *non*magnetic dopants leading to room-temperature ferromagnetic behavior is arguably even more interesting. To date, room-temperature ferromagnetism (RTFM) has been reported experimentally for carbon doped ZnO,[6,7] lithium doped ZnO,[8] nitrogen doped ZnO[9] and TiO$_2$,[10] and carbon doped In$_2$O$_3$,[11] to name a few. Such "d^0" magnetic materials are often considered more desirable than those with 3d dopants because issues such as metallic clustering and phase segregation can be avoided more easily (though it is still subjective at this point to say one class is strictly better than the other).

Several explanations for the mechanisms behind ferromagnetism in DMSs doped with nonmagnetic atoms have been explored. Some experimental studies highlight a link between anion vacancies and induced ferromagnetism in d^0 systems.[12] Such vacancies can have the effect of introducing spin split impurity bands,[13] or the vacancies can simply lead to local distortions and large local moments with longer-range coupling capabilities. At the same time, however, some theoretical studies of carbon and nitrogen doped ZnO found that the introduction of oxygen vacancies did not induce ferromagnetism.[14] Another explanation, developed using a theoretical and experimental approach, suggested that cation (Zn) vacancies in lithium doped ZnO were intimately linked with room-temperature ferromagnetism.[8] Thus, it is clear that the magnetic properties of these materials are very sensitive to the constituent species and the various synthesis parameters and as such more studies are needed to fully understand the mechanisms.

In this work we study the ferromagnetic semiconductor carbon doped In$_2$O$_3$ (In$_2$O$_3$:C). While numerous studies of transition-metal dopants in In$_2$O$_3$ have been carried out (with dopants including Fe,[5,15–17] Co,[18] Ni,[19] and Cu[20]), fewer studies have been performed involving nonmagnetic dopants.[11,21] Here, we first employ density-functional theory modeling to study the electronic structures and magnetic properties of various possible defect configurations. Next, we utilize soft x-ray emission spectroscopy (XES) and absorption spectroscopy (XAS) to study the element specific electronic structures of a set of In$_2$O$_3$:C materials. Previous experimental studies for the samples studied here have revealed ferromagnetism at room temperature for some of the samples, with varied magnetic behavior for different dopant concentrations and synthesis conditions. We find through theory and experiment that a key

ingredient to ferromagnetic behavior is p-p coupling brought about by unpaired electrons on substitutional dopant atoms. A strong C $2p$ contribution to the density of states (DOS) at the Fermi level, as well as C $2sp$ and In $4d$ hybridization, are characteristics of this behavior which were confirmed experimentally. Further, we show that these key electronic structure features can be realized through a combination of interstitial C atoms and substitutional C atoms at oxygen sites.

II. COMPUTATIONAL AND EXPERIMENTAL DETAILS

The electronic structure calculations reported within this work are density-functional theory (DFT) calculations performed using the SIESTA pseudopotential code,[22] as utilized with success previously for related studies of impurities in semiconductors.[23] All calculations were performed using the Perdew-Burke-Ernzerhof variant of the generalized gradient approximation (GGA-PBE)[24] for the exchange-correlation potential. A full optimization of the atomic positions was performed during which the electronic ground state was consistently found using norm-conserving pseudopotentials for cores and a double-ζ plus polarization basis of localized orbitals for In, C, and O. Optimizations of the force and total energy were performed with an accuracy of 0.04 eV/Å and 1 meV, respectively. For the atomic structure calculations we employed an In pseudopotential with In $4d$ electrons in the core. For the plots of In $4d$ densities of states we used the obtained crystal structure and performed the electronic structure calculations while taking into account the occupied orbitals. All calculations were performed with an energy mesh cutoff of 360 Ry and a k-point mesh of $6 \times 6 \times 6$ in the Mokhorst-Park scheme.[25]

The calculations of the formation energies (E_{form}) were performed using the standard method described in detail in Ref. 23. The Curie temperatures (T_C) were estimated using the formula

$$T_C = \frac{JS(S+1)}{3k_B},\qquad(1)$$

where J is the exchange interaction, S is the total spin of the defect clusters, and k_B is the Boltzmann constant. The values of the exchange interactions between the clusters are calculated by the formula

$$J = \frac{E_{\text{AFM}} - E_{\text{FM}}}{2S^2},\qquad(2)$$

where E_{FM} and E_{AFM} are the total energies for parallel and antiparallel orientation of spins on the remote clusters, respectively.

To understand the nature of the ferromagnetism in the materials, different combinations of structural defects were calculated in the In_2O_3 matrix. As a host for the studied defects we used an In_2O_3 supercell consisting of 80 atoms ($In_{32}O_{48}$). Taking into account our previous modeling of transition-metal and aluminum impurities in semiconductors,[23] we have performed calculations for various combinations of substitutional (S) and interstitial (I) carbon impurities, and have also considered the presence of oxygen vacancies (V_O).

The physical In_2O_3:C samples studied in this work are thin films that were deposited on Si (100) substrates by radio

frequency (RF) magnetron cosputtering of In_2O_3 and carbon targets. For different samples, the deposition process was carried out at room temperature and 550 °C, respectively, to test the effects of synthesis temperature on the final materials. The RF power on the In_2O_3 target was maintained at 50 W, while the RF power on the carbon target was varied for different films to obtain varying carbon concentration in the final products. Prior to deposition, the base pressure of the chamber was kept below 4 x 10^{-6} Pa at room temperature. The deposition was performed under 1.5 Pa of Ar gas pressure.

Structural characterization of the In_2O_3:C films was carried out using an x-ray diffractometer (XRD, Bruker AXS: D8 ADVANCE) with a working current and voltage of 40 mA and 40 kV, respectively. Carbon concentrations were determined using both energy-dispersive x-ray spectroscopy (EDX) and Rutherford backscattering spectroscopy (RBS). The magnetic properties of the films were investigated with a vibrating sample magnetometer (VSM) attached to a Quantum Design physical property measurement system (PPMS). The measurements were performed at 300 K with a field parallel to the thin-film planes ranging in strength from -1 to 1 T. Further details and a complete discussion of the results of these initial characterization procedures can be found in Refs. 11 and 21.

The x-ray emission spectroscopy (XES) and resonant XES (RXES) measurements of the carbon and oxygen K edges were performed using Beamline 8.0.1[26] of the Advanced Light Source (ALS) at Lawrence Berkeley National Laboratory. The beamline uses a Rowland circle type grating spectrometer with spherical gratings. The emitted photons from the sample are detected at an angle of 90° to the incident photons, and for these experiments the incident photons impinged at 30° to the sample surface normal with linear polarization in the horizontal scattering plane. The experiments were performed in a vacuum chamber at $\sim 10^{-9}$ Torr. The x-ray absorption spectroscopy (XAS) measurements were performed using the SGM beamline[27] of the Canadian Light Source (CLS). Linear photon polarization was used, and the XAS was measured via total electron yield (TEY) mode at a vacuum pressure of $\sim 10^{-8}$ Torr.

III. RESULTS

A. DFT modeling

Structural visualizations for a subset of the defect configurations which were modeled are shown in Fig. 1. Note that these are local configurations which were situated in the supercell described above to replicate the dilute doping scenario. The configurations shown in the figure are optimized structures for the various defect cases. Throughout this work, defect structures consist of different combinations of substitutional (S) carbon atoms at O sites, interstitial (I) carbon atoms, and oxygen vacancies (V_O). For each defect configuration, the density of states (DOS), formation energy, magnetic moment, and Curie temperature (T_c, where applicable) were calculated.

1. Substitutional (S) carbon

We consider first the simplest case of a single substitutional carbon atom, as depicted in panel (a) of Fig. 1. The calculated formation energy for this case is quite large ($\sim$8 eV, see
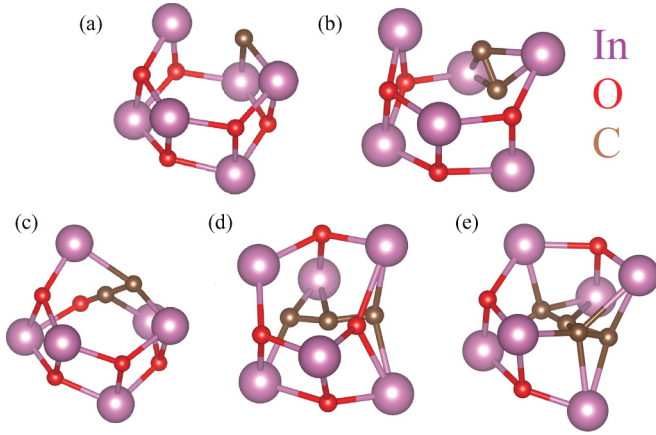
FIG. 1. (Color online) Optimized local defect structures for (a) single substitutional carbon, (b) two substitutional carbons, (c) one substitutional and one interstitial carbon, (d) two substitutional carbons and one interstitial carbon, and (e) three substitutional carbons and one interstitial carbon.

Table I), and in close agreement with previous theoretical results.[28] In this case the C atom maintains two unpaired electrons, as the C atom with a formal valence of -4 replaces the O atom with a valence of -2. These unpaired electrons lead to a small net magnetic moment, as shown in Table I. The density of states (DOS) for this configuration is shown in Fig. 2(a). We see that due to the unpaired electrons there is strong C $2p$ character at the Fermi level, and localized C $2s$ states deeper in the valence band (~ -10 eV).

If we consider increasing the carbon concentration while retaining only substitutional configurations, we reach the regime where the C atoms are near each other and may interact directly. This is represented by the $2S$ configuration, as depicted in Fig. 1(b). In this case, the unpaired electrons which were present in the $1S$ case form a double bond between the two substitutional carbon atoms. This elimination of the unpaired $2p$ electrons leads to a significant reduction in the formation energy, now down to 4.98 eV, as shown in Table I. Additionally, the formation of the double bond eliminates the strong C $2p$ character near the Fermi level in the DOS, as shown in Fig. 2(b), and eliminates the magnetic moment.

TABLE I. Calculated formation energies and magnetic properties for different configurations of structural defects in In$_2$O$_3$:C. Results for the structural defects with the inclusion of oxygen vacancies are shown in parentheses. Hyphens indicate values of zero.

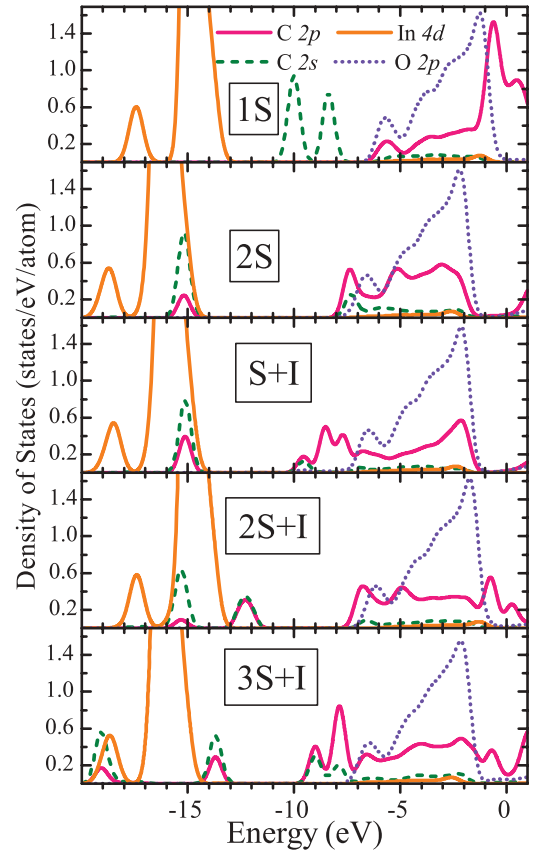| Impurity	C (%)	E_{form} (eV)	Mag. mom. (μ_B/C)	J (meV)	T_C (K)
$1S$	2	$+7.78\ (+6.36)$	$2.26(-)$	$+1(-)$	$55(-)$
$2S$	4	$+4.98\ (+4.85)$	$-(-)$	$-$	$-$
$4S$	8	$+4.84\ (+4.80)$	$-(-)$	$-$	$-$
I	2	$+4.08\ (+4.08)$	$-(-)$	$-$	$-$
$S+I$	4	$+3.11\ (+3.09)$	$-(-)$	$-$	$-$
$2S+I$	**6**	**$+3.91\ (+3.82)$**	**$0.33(-)$**	**$+8\ (-)$**	**$279\ (-)$**
$3S+I$	8	$+4.37\ (+4.08)$	$-(-)$	$-$	$-$
$4S+I$	10	$+4.42\ (+4.26)$	$-(-)$	$-$	$-$
$6S+I$	14	$+4.28\ (+4.15)$	$-(-)$	$-$	$-$

FIG. 2. (Color online) The calculated densities of states per atom for different types of carbon structural defects in In$_2$O$_3$.

Finally, the double bond between the C atoms shifts them from the original lattice positions and induces a hybridization between the C $2sp$ states and the In $4d$ states, as shown in the region around -15 eV. This hybridization becomes evident in all cases where structural distortions of the In octahedra near C atoms are present, as discussed in more detail below. We note that the consideration of a further increase in carbon concentration to the $4S$ case has little effect on the formation energy and still exhibits no magnetic behavior (see Table I).

2. Interstitial (I) + substitutional (S) carbon

With only a weak predicted magnetic moment for substitutional carbon, and a relatively high formation energy, we next consider the effects due to the introduction of interstitial carbon atoms in the In$_2$O$_3$ lattice. The results for the case of only interstitial carbon are summarized in Table I. A slight reduction in the formation energy is found compared to the substitutional cases described above. However, no net magnetic moment is found, suggesting that purely interstitial C does not lead to RTFM in In$_2$O$_3$:C.

When one considers varying amounts of substitutional C atoms in addition to the interstitial C ($xS + I$), the results are quite different. Here, the x substitutional atoms are grouped around a C atom in the fairly spacious interstitial region of the cluster. As seen from the optimized structures of the $xS + I$ clusters in Figs. 1(c)–1(e), a strong interaction is present between the interstitial C atom and one of the In atoms in each case. This interaction leads to a shift of the interstitial C atom
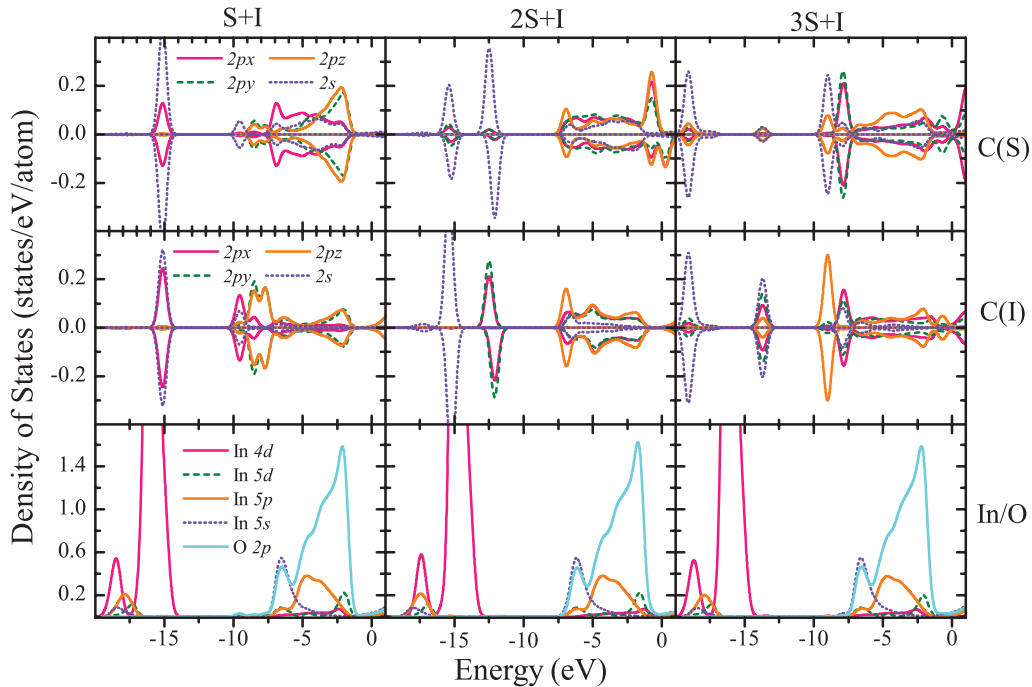
FIG. 3. (Color online) Partial densities of states (PDOS) for the different substitutional and interstitial configurations. The three columns are for the $1S + I$, $2S + I$, and $3S + I$ cases from left to right, respectively. The three rows show, for each configuration, the spin-projected PDOS for the substitutional [C(S)] and interstitial carbon atoms [C(I)] and the PDOS for the In and O atoms (In/O).

from the center of the interstitial region to a location closer to an In atom. The prominence of this shift is due to the freedom of the interstitial atom in the large interstitial region as opposed to the more constricted substitutional C atoms.

As with the $2S$ case described above, the interaction of the interstitial atom and one of the In atoms accompanies a slight structural distortion and consequently leads to the presence of low-energy peaks in the calculated DOS (Fig. 2) due to the hybridization of the carbon $2sp$ states and the In $4d$ semicore states around -15 eV. This effect is accompanied by a further reduction in formation energies from the purely substitutional cases (Table I). Additionally, as shown in the table, the $2S + I$ cluster leads to a strong magnetic moment with a calculated T_C near room temperature. Referring back to Fig. 2, the $2S + I$ case also shows the strongest combination of C $2sp$-In $4d$ mixing and C $2p$ states near the Fermi level, similar to the $1S$ case.

To examine in more detail the electronic structure of these $xS + I$ configurations, spin-polarized and site-projected partial DOS are shown in Fig. 3. The results for the $1S + I$, $2S + I$, and $3S + I$ configurations are shown in the left, middle, and right columns of the figure, respectively, and the DOS for the substitutional carbon, interstitial carbon, and host lattice atoms are shown in the upper, middle, and lower rows, respectively. Here we see that it is indeed the interstitial C atoms which hybridize most strongly with the In $4d$ states. Additionally, the presence of $2p$ states at the Fermi level is evident for the substitutional atoms in the $2S + I$ case. These features are discussed in further detail in Sec. IV below.

3. Oxygen vacancies (V_O)

Finally, for each of the configurations studied above, we have considered via calculations the presence of oxygen

vacancies and their effect on the electronic structure and magnetic properties. The role of oxygen vacancies is a prominent research theme in many recent studies of dilute magnetic semiconductors. Earlier studies of the samples described later in this work indicated oxygen vacancies may play an important role in mediating the ferromagnetism, so it is crucial to study their impact theoretically as well.

The results from the inclusion of oxygen vacancies in the DFT calculations are summarized in the parenthesized values of Table I. Interestingly, in all cases—even the ones which showed ferromagnetic ordering without vacancies— no ferromagnetic behavior was calculated for the defect configurations when vacancies were included. For each case, the lowest formation energy was found when oxygen vacancies were placed nearest to the C atoms, and consequently it is these cases for which the results are reported.

Figure 4 shows the calculated DOS for two example cases where V_O were included, specifically the $1S + V_O$ and $2S + V_O$ cases. For direct comparison, the C $2p$ states for the $1S$ and $2S$ cases of Fig. 2 are shown as well in shaded gray. Noting that the introduction of V_O leads to the presence of an additional two unpaired electrons, we find that for $1S + V_O$ these electrons are passivated by the two unpaired electrons on the carbon impurity. The consequent absence of unpaired electrons for this situation then leads to a vanishing of the magnetic moment and a modification of both the C $2p$ states near the Fermi level and the C $2s$ semivalence states at about -9 eV. This is evident in the upper panel of Fig. 4. For the C $2p$ DOS, there is no longer a strong peak immediately above the Fermi level (as was the case for $1S$ due to the unpaired electrons), and instead only the tail of the lower peak crosses E_F. For the C $2s$ DOS, the two peaks that were present
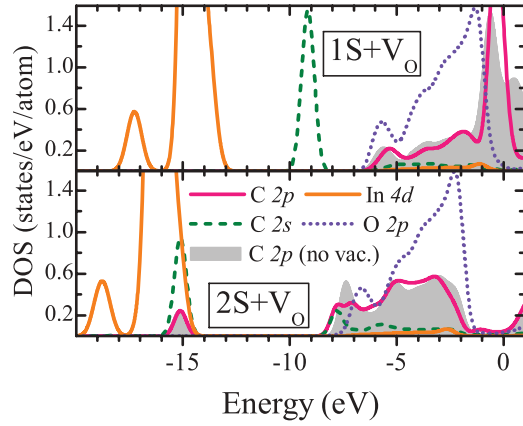
FIG. 4. (Color online) The calculated densities of states per atom for different types of carbon structural defects in In_2O_3 which include an oxygen vacancy. For comparison, the C $2p$ states are shown in light shaded gray for the case with no vacancy as well.

in the -8 to -10 eV region for the $1S$ case have changed and now only one peak is present. These $2s$ states retain their noninteracting semivalence character, as there is still no hybridization with the In $4d$ states, but they have merged into one peak due to the absence of the unpaired electrons.

The lower panel of Fig. 4 shows the results for the $2S + V_O$ case. Here, the electrons introduced by the V_O lead to the conversion of the C=C double bond to a single bond, and a light shift of the C states from the Fermi level is observed. The $2S + V_O$ case remains nonmagnetic.

B. Experimental results

To study the electronic structure of In_2O_3:C experimentally and thus test the DFT modeling predictions, soft x-ray emission spectroscopy (XES) and x-ray-absorption spectroscopy (XAS) were employed. When applied to the C and O K edges, these techniques probe the C and O $2p$ occupied (XES) and unoccupied (XAS) DOS. Here, three films of In_2O_3:C were studied: one with 4.5 at. % carbon prepared at room temperature (300 K) which exhibited ferromagnetic behavior (saturation magnetization $M_s \approx 4.9$ emu/cm^3 or 0.15 μ_B/C), one with 9.3% carbon prepared at room temperature which showed reduced ferromagnetic behavior ($M_s \approx 1.8$ emu/cm^3 or 0.03 μ_B/C), and one with 4.0% carbon prepared at 550 °C which again exhibited weaker ferromagnetism ($M_s \approx 1.0$ emu/cm^3 or 0.04 μ_B/C). Magnetization curves for the three samples are shown in Fig. 5. The inset shows an enlarged view of the full hysteresis loop for the sample exhibiting the strongest FM, for visualization purposes. As noted in our earlier work,[11,21] films prepared with no C doping exhibited no ferromagnetism, verifying that the C doping was indeed responsible for the induced magnetic properties.

The C K-edge XES spectra, which probe the occupied C $2p$ DOS, are shown in the lower panel of Fig. 6. We note first that due to the dilute C content and high oxygen concentration of the samples, as well as the nature of grating spectroscopy, an artificial peak from the O K XES detected in second diffraction order was necessarily subtracted from all the C K XES and RXES. For the 4.5% concentration sample synthesized at room
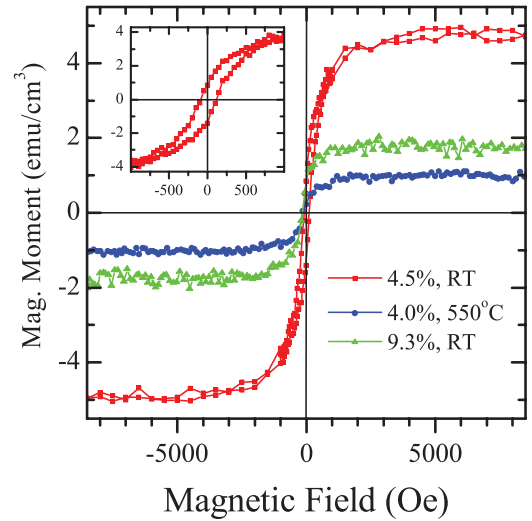

FIG. 5. (Color online) Magnetization curves of the In_2O_3:C films studied. Inset: expanded full hysteresis loop for the 4.5% sample prepared at room temperature.

temperature, the raw data with this artificial peak are shown in the left inset. For materials with high C concentrations or without oxygen, this is not typically an issue, but here
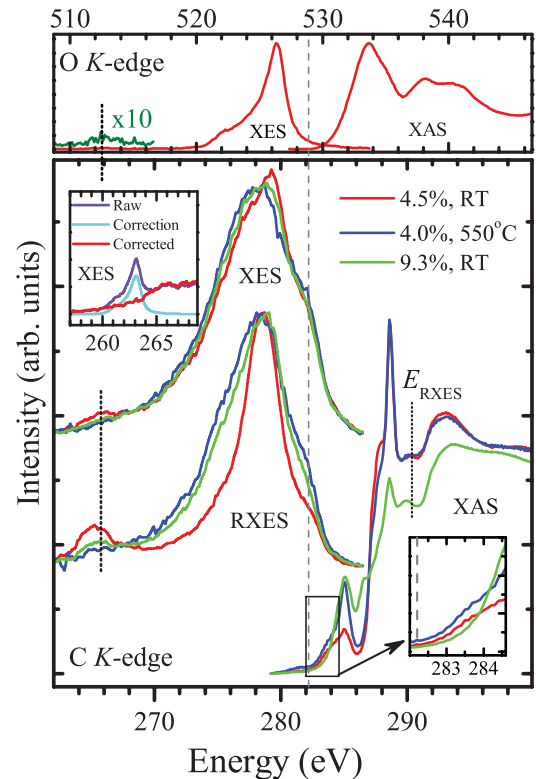

FIG. 6. (Color online) X-ray spectroscopy results for the In_2O_3:C samples described in the text. Carbon K-edge XES, RXES, and XAS are shown in the main lower portion of the figure. Left inset: correction necessary to remove the second-order oxygen signal. Right inset: magnified view of the XAS onset. The upper plot shows the oxygen K-edge XES and XAS of one sample to display the similar In $4d$ to anion $2sp$ hybridization seen for both the O and C anions, as well as the host DOS in the band-gap region.

care needed to be taken to correct for the artifact. Separate measurements of the oxygen K edge taken during the same experiment enabled the precise subtraction of this spectral component. This is shown in the aforementioned inset, where the O K XES is shown on a halved energy scale (to account for second-order diffraction) and subtracted from the raw data to give the final spectrum. It is these corrected spectra which are shown in the main portion of the figure.

With the spectra properly corrected, a key feature becomes evident in the region around $\sim$265.4 eV. Here, the presence of hybridization between the C $2sp$ and the In $4d$ semicore electrons can be detected, in the expected energy range of 15–18 eV below the Fermi level. In particular, the 4.5% doped sample prepared at room temperature (which possesses the highest magnetic moment) exhibits the most prominent C $2sp$-In $4d$ hybridization. This hybridization feature is enhanced in the RXES spectra, which are excited at E_{RXES} as labeled on the XAS spectra. This enhancement in the RXES shows more clearly that the 4.5% doped RT sample has the strongest hybridization, while the 9.3% doped RT sample has the next strongest, and the 4.0% doped sample prepared at 550 °C shows very little hybridization.

The O K-edge XES and XAS for the 4.5% doped sample prepared at room temperature are shown in the upper panel of Fig. 6. The O spectra are very similar for the various samples and for an undoped In_2O_3 reference sample, so only one set is shown in the figure for clarity. This similarity for all samples verifies that the In_2O_3 host matrices are identical for all doping cases. Note that the doped C atoms are expected to have a very minor effect on the O spectra due to the dilute nature, which explains why no variations between samples were found. The O spectra in the figure are displayed on a translated (but nonscaled) energy scale to line up vertically with the C spectra below on a binding-energy scale. This can be achieved via the semicore In $4d$ hybridization peak in both spectra (black, dotted lines near the left side in each plot), which serves as a reference for alignment of the valence band.

With the C and O XES spectra aligned on a common binding-energy scale in Fig. 6, the relative positioning of the C and O $2p$ states within the valence band can be discerned. With the gray, vertical dashed line used to denote the top of the O $2p$ contribution (and thus the approximate Fermi level for the host In_2O_3), we indeed see a strong C $2p$ contribution to the very top of the valence band. For the sample exhibiting the strongest ferromagnetism (4.5% doping, RT synthesis), we see a further shift of the C $2p$ spectral weight toward the Fermi level. This is in agreement with the DFT calculations, which showed that the unpaired C(S) electrons in the magnetic $2S + I$ case led to a strong C $2p$ presence at the Fermi level.

Finally, in the lower right portion of Fig. 6, we plot the C K-edge XAS spectra for the samples. Comparing to the O K-edge XAS above, it is evident that some unoccupied C $2p$ states are present within the In_2O_3 band gap for all samples. Closely examining the XAS onset via the inset in the lower right, we see the two samples with lower doping levels have similar onsets (with the sample synthesized at 550 °C having a slightly stronger onset)—essentially beginning right above the Fermi level approximated by the dashed vertical line—while the 9.3% doped sample onsets at a higher energy, indicating

the unoccupied C $2p$ states begin further above the Fermi level for this sample.

IV. DISCUSSION

Additional insight can be gained into the magnetic properties and electronic structure of In_2O_3:C by considering the bonding characteristics of the various defect structures, determined from valence considerations and the calculated DOS, and shown in Fig. 7. First, we note again the unpaired electrons present in the $1S$ case, which is shown in Figs. 1(a) and 7(a). Note that unpaired electrons are shown as green circles in Fig. 7. As mentioned earlier, these unpaired electrons lead to the presence of a strong peak at the Fermi level, which enables the exchange between defects, even at a distance of about 1 nm. However, it is noted that the T_C in this case is quite low. Additionally, the formation energy is quite high, suggesting that such configurations would not likely be attained via synthesis at room temperature.

To understand the nature of the magnetism in the $2S + I$ cluster and its absence from the other clusters, we can again consider in more detail the chemical bonding. First, in the case of the $1S + I$ cluster, a double bond between the two carbon atoms is formed, and each of the carbon atoms has two single bonds with the neighboring In and O atoms [see Fig. 7(c)]. There are no unpaired electrons for this cluster, and recall that no magnetism was present for the calculations of this cluster. In the case of the more complex $3S + I$ cluster, each carbon atom forms four single bonds, with other carbon atoms and indium atoms. As a consequence of this, there is again an absence of magnetism for this configuration. It is of note for this case, though, that the C $2sp$–In $4d$ hybridization is weaker (c.f. Fig. 3) compared to the other cases where hybridization is present. Accordingly, there is some weight in the DOS near the Fermi level, but not enough to support magnetism.

Finally, for the case of the magnetic $2S + I$ cluster, we consider first that each carbon atom forms three single bonds with neighboring C and In atoms. This leaves the ability for the formation of a double bond between the interstitial C and one of the substitutional C atoms (see Fig. 7). When this double
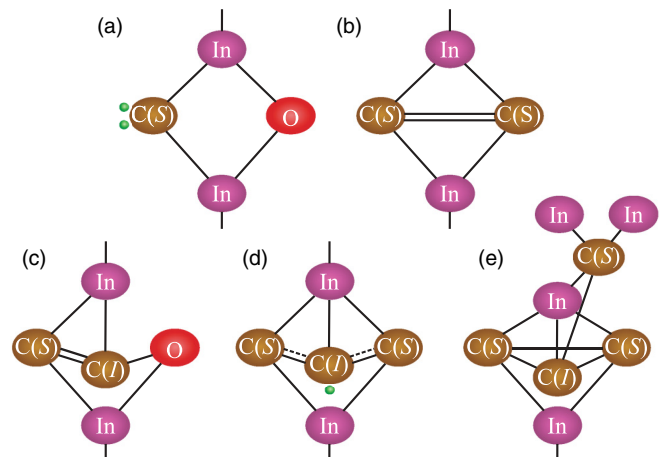

FIG. 7. (Color online) Chemical bonding diagrams for the defect clusters considered in the calculations. (a–e) $1S$, $2S$, $1S + I$, $2S + I$, and $3S + I$ cases, respectively.

bond forms with one C(S), the result is a single unpaired electron on the other substitutional C atom. The effects of this behavior can be seen in the DOS of Fig. 3. For the $2S + I$ cluster, the electronic structure of the C(I) atom is close to that of the $S + I$ cluster: the C $2p$ states are similar, and there is strong C $2sp$-In $4d$ hybridization. The presence of the unpaired electron in one of the C(S) sites for $2S + I$ is also confirmed with the strong C $2p$ weight at the Fermi level, similar to the $1S$ situation of Fig. 2, where two unpaired electrons were present. Finally, note that the magnetic moment of 0.33 μ_B/C calculated for the $2S + I$ and shown in Table I corresponds to the single unpaired electron per cluster of three C atoms. The exchange value of 8 meV is comparable to other DFT works looking at C doped ZnO[29] and N doped In$_2$O$_3$,[30] which found values of $\sim$5–10 meV for spins separated by a comparable $\sim$6–10 Å.

With the considerations above, the magnetism present in the $2S + I$ calculation can be attributed to the p-p coupling mechanism, which has been suggested for the similar case of ZnO:C.[6,7,31] The unpaired C(S) $2p$ electrons which do not participate in the ordinary C-C, C-In, or double C=C bonds act to form an impurity band near the Fermi level. The resultant strong DOS at the Fermi level allows for the long-ranged p-p exchange mechanism to act between the distant clusters.

Returning to the physical samples and experimental results, the above discussion helps to explain why the samples exhibited varying magnetic behavior. First, if we consider the 4.5% doped sample prepared at room temperature, a strong C $2sp$-In $4d$ hybridization was found in the C K-edge XES spectrum (Fig. 6). Additionally, there was a strong presence of C $2p$ states near the Fermi level in both the XES and XAS (though not quite as strong as for the sample prepared at high temperature). These observations suggest that there is a presence of both C(I) (leading to the hybridization) and unpaired electrons (leading to spectral weight at the Fermi level) similar to the $2S + I$ cluster DFT results and thus indicate why the magnetism was strongest for this case.

If we consider the 4.0% doped sample prepared at 550 °C, we see that the C $2sp$-In $4d$ hybridization is almost completely absent from the XES and RXES, but there is still a very strong C $2p$ presence at the Fermi level in the XES and XAS. These results suggest that this sample likely contains single substitutional C atoms (the $1S$ configuration), as the calculated DOS for this case showed no hybridization but strong C $2p$ states at the Fermi level due to unpaired electrons. In fact, the $1S$ configuration has more states at the Fermi level than the $2S + I$ configuration (see Fig. 2), just as this sample has more such states than the 4.5%, RT sample. Next, recalling from Table I that the $1S$ case had a very low T_C, it is understandable that this corresponding sample had a very weak magnetism ($M_S = 0.04\mu_B$/C). Additionally, noting the higher formation energy for the $1S$ case in Table I, it is understandable that synthesis at a higher temperature would lead to more $1S$ sites.

Finally, with increased doping to 9.3%, there appears to be a moderate amount of C(I) atoms, as there is a weak hybridization feature in the XES. Additionally, the XAS shows that the unoccupied C $2p$ states have moved away

from the Fermi level compared to the other samples. This indicates that although there is hybridization, we have a lack of unpaired electrons in this sample to facilitate magnetism. Such a situation is likely due to the higher concentration, leading to more C atoms near each other, which can reduce the number of unpaired electrons through configurations like the $2S$ case. The combination of features described above explains why this sample has very weak magnetism ($M_S = 0.03\mu_B$/C). Thus, for all three experimental samples, the combination of XES/XAS spectra and DFT results are able to explain the relative magnetic moments.

It is worth noting that earlier studies suggested V_O might be responsible for RTFM in films of In$_2$O$_3$:C.[11,21] This suggestion was proposed because annealing in O$_2$ was found to reduce the magnetism in the films. Our results lead to an alternative explanation: annealing could convert magnetic defect configurations (such as $2S + I$) into $1S$ configurations, thereby suppressing the magnetic properties of the films. Note, however, that these results do not rule out the importance of V_O in other materials, including undoped In$_2$O$_3$ surfaces[32] and nanoparticles.[33]

V. CONCLUSION

To conclude, we have conducted a theoretical and experimental study of the magnetism in carbon doped In$_2$O$_3$. Density-functional theory calculations showed that ferromagnetism is possible near room temperature if a combination of substitutional and interstitial carbon impurities is present. Such a configuration leads to unpaired C $2p$ electrons at substitutional sites which produce local magnetic moments and states near the Fermi level. Via these states near the Fermi level, a p-p coupling interaction mediates the magnetism. Additionally, in such a situation, a strong hybridization between the In $4d$ states and the C $2sp$ states was predicted via DFT due to interstitial atoms migrating near In atoms. These electronic structure attributes were confirmed experimentally using x-ray spectroscopy experiments on a set of samples with varied synthesis properties and magnetic behavior. The theoretical and experimental results combine to provide a comprehensive explanation for the magnetic behavior of the material.

*robert.green@usask.ca

[1] S. Wolf, D. Awschalom, R. Buhrman, J. Daughton, S. von Molnar, M. Roukes, A. Chtchelkanova, and D. Treger, Science **294**, 1488 (2001).

[2] S. Ogale, Adv. Mater. **22**, 3125 (2010).

[3] J. M. D. Coey, M. Venkatesan, and C. B. Fitzgerald, Nat. Mater. **4**, 173 (2005).

[4] G. Ciatto, A. Di Trolio, E. Fonda, P. Alippi, A. M. Testa, and A. A. Bonapasta, Phys. Rev. Lett. **107**, 127206 (2011).

[5] S. Qi, F. Jiang, J. Fan, H. Wu, S. B. Zhang, G. A. Gehring, Z. Zhang, and X. Xu, Phys. Rev. B **84**, 205204 (2011).

[6] H. Pan, J. B. Yi, L. Shen, R. Q. Wu, J. H. Yang, J. Y. Lin, Y. P. Feng, J. Ding, L. H. Van, and J. H. Yin, Phys. Rev. Lett. **99**, 127201 (2007).

[7] S. Zhou, Q. Xu, K. Potzger, G. Talut, R. Grotzschel, J. Fassbender, M. Vinnichenko, J. Grenzer, M. Helm, H. Hochmuth, M. Lorenz, M. Grundmann, and H. Schmidt, Appl. Phys. Lett. **93**, 232507 (2008).

[8] J. B. Yi, C. C. Lim, G. Z. Xing, H. M. Fan, L. H. Van, S. L. Huang, K. S. Yang, X. L. Huang, X. B. Qin, B. Y. Wang, T. Wu, L. Wang, H. T. Zhang, X. Y. Gao, T. Liu, A. T. S. Wee, Y. P. Feng, and J. Ding, Phys. Rev. Lett. **104**, 137201 (2010).

[9] C.-F. Yu, T.-J. Lin, S.-J. Sun, and H. Chou, J. Phys. D: Appl. Phys. **40**, 6497 (2007).

[10] N. N. Bao, H. M. Fan, J. Ding, and J. B. Yi, J. Appl. Phys. **109**, 07C302 (2011).

[11] K. B. Ruan, H. W. Ho, R. A. Khan, P. Ren, W. D. Song, A. C. H. Huan, and L. Wang, Solid State Commun. **150**, 2158 (2010).

[12] G. Xing, D. Wang, J. Yi, L. Yang, M. Gao, M. He, J. Yang, J. Ding, T. C. Sum, and T. Wu, Appl. Phys. Lett. **96**, 112511 (2010).

[13] J. Coey, Solid State Sci. **7**, 660 (2005).

[14] A. Pham, M. H. N. Assadi, Y. B. Zhang, A. B. Yu, and S. Li, J. Appl. Phys. **110**, 123917 (2011).

[15] X.-H. Xu, F.-X. Jiang, J. Zhang, X.-C. Fan, H.-S. Wu, and G. A. Gehring, Appl. Phys. Lett. **94**, 212510 (2009).

[16] S. C. Li, P. Ren, B. C. Zhao, B. Xia, and L. Wang, Appl. Phys. Lett. **95**, 102101 (2009).

[17] R. K. Singhal, A. Samariya, S. Kumar, S. C. Sharma, Y. T. Xing, U. P. Deshpande, T. Shripathi, and E. Saitovitch, Appl. Surf. Sci. **257**, 1053 (2010).

[18] A. M. H. R. Hakimi, M. G. Blamire, S. M. Heald, M. S. Alshammari, M. S. Alqahtani, D. S. Score, H. J. Blythe, A. M. Fox, and G. A. Gehring, Phys. Rev. B **84**, 085201 (2011).

[19] R.-R. Ma, F.-X. Jiang, X.-F. Qin, and X.-H. Xu, Mater. Chem. Phys. **132**, 796 (2012).

[20] Z. G. Yu, J. He, S. Xu, Q. Xue, O. M. J. van't Erve, B. T. Jonker, M. A. Marcus, Y. K. Yoo, S. Cheng, and X.-D. Xiang, Phys. Rev. B **74**, 165321 (2006).

[21] R. A. Khan, A. S. Bhatti, and R. K., J. Magn. Magn. Mater. **323**, 2841 (2011).

[22] J. Soler, E. Artacho, J. Gale, A. Garcia, J. Junquera, P. Ordejon, and D. Sanchez-Portal, J. Phys.: Condens. Matter **14**, 2745 (2002).

[23] G. S. Chang, E. Z. Kurmaev, D. W. Boukhvalov, L. D. Finkelstein, S. Colis, T. M. Pedersen, A. Moewes, and A. Dinia, Phys. Rev. B **75**, 195215 (2007).

[24] J. P. Perdew, K. Burke, and M. Ernzerhof, Phys. Rev. Lett. **77**, 3865 (1996).

[25] H. Monkhorst and J. Pack, Phys. Rev. B **13**, 5188 (1976).

[26] J. Jia, T. Callcott, J. Yurkas, A. Ellis, F. Himpsel, M. Samant, J. Stohr, D. Ederer, J. Carlisle, E. Hudson, L. Terminello, D. Shuh, and R. Perera, Rev. Sci. Instrum. **66**, 1394 (1995).

[27] T. Regier, J. Krochak, T. Sham, Y. Hu, J. Thompson, and R. Blyth, Nucl. Instrum. Methods Phys. Res. A **582**, 93 (2007).

[28] R. Long and N. English, J. Phys. Chem. C **114**, 13942 (2010).

[29] S. K. Nayak, M. E. Gruner, S. Sakong, S. Sil, P. Kratzer, S. N. Behera, and P. Entel, Phys. Rev. B **86**, 054441 (2012).

[30] L. X. Guan, J. G. Tao, C. H. A. Huan, J. L. Kuo, and L. Wang, Appl. Phys. Lett. **95**, 012509 (2009).

[31] X. Wang, X. Chen, R. Dong, Y. Huang, and W. Lu, Phys. Lett. A **373**, 309 (2009).

[32] Z. R. Xiao, X. F. Fan, L. X. Guan, C. H. A. Huan, J. L. Kuo, and L. Wang, J. Phys.: Condens. Matter **21**, 272202 (2009).

[33] A. Sundaresan, R. Bhargavi, N. Rangarajan, U. Siddesh, and C. N. R. Rao, Phys. Rev. B **74**, 161306 (2006).